ENGINEERING

Network topology–directed design of molecular CPU for cell-like dynamic information processing

Dan Wang[1], Yani Yang[1], Fengming Chen[1], Yifan Lyu[1,2]*, Weihong Tan[1,3,4]*

Natural cells (NCs) can automatically and continuously respond to fluctuant external information and distinguish meaningful stimuli from weak noise depending on their powerful genetic and protein networks. We herein report a network topology–directed design of dynamic molecular processing system (DMPS) as a molecular central processing unit that powers an artificial cell (AC) able to process fluctuant information in its immediate environment similar to NCs. By constructing a mixed cell community, ACs and NCs have synchronous response to fluctuant extracellular stimuli under physiological condition and in a blood vessel–mimic circulation system. We also show that fluctuant bioinformation released by NCs can be received and processed by ACs. The molecular design of DMPS-powered AC is expected to allow a profound understanding of biological systems, advance the construction of intelligent molecular systems, and promote more elegant bioengineering applications.

INTRODUCTION

Natural cells (NCs) can adapt to an ever-changing biological environment and initiate specific cellular responses by continuously receiving and processing extracellular information, depending on their biochemical reaction networks (*1*, *2*). Meanwhile, by establishing a stimulus threshold, NCs can discriminate meaningful stimuli from weak noise, to prevent, for example, the unintentional activation of signaling pathways through background fluctuations (*3*, *4*). Over the past decade, the fields of synthetic biology and system biology have invested great efforts to engineer synthetic NC-like artificial system using cascading reactions that can reprogram or mimic cellular functions such as self-adaption (*5*, *6*), cell-cell communications (*7*, *8*), predatory behaviors (*9–11*), and metabolic pathways (*12*, *13*), for better understanding of network properties behind these cellular systems (*14–16*). However, it is still a big challenge to construct synthetic systems that can dynamically sense and process meaningful stimuli instead of background noise in a manner equal to NCs. This is because these complex and dynamic system behaviors can only be implemented on the basis of well-organized network topologies instead of simple reactions, according to studies about dynamic cell behaviors such as noise filtering in bacteria and stem cell differentiation (*17*, *18*).

DNA reaction networks (DRNs) offer a flexible bridge between abstract network topology and concrete chemical building blocks (*6*, *19–24*). With such merits as easy chemical synthesis, strict base pairing, precise molecular programmability, and favorable biorecogniton capability, several DRN-functionalized artificial systems have been reported by our group and others including simulation of artificial immune response (*25*, *26*), evaluation of protein expression (*27*), mimicry of signal pathway (*28*), and self-adaptive regulation of enzyme activity (*29*, *30*). These works demonstrate the robust logic controlling ability of DRNs and encourage us to engineer more sophisticated artificial systems with complex NC-like behaviors.

Inspired by the network topology of biological systems, here, we show that NC-like dynamic information processing can be realized by a DRN system integrating four incoherent feedforward loops (FFLs) and a threshold gate. This whole system, termed the dynamic molecule processing system (DMPS), is further built as the molecular central processing unit (mCPU) of artificial cells (ACs), enabling ACs to sense, analyze, and process continuous fluctuation of extracellular stimuli. The AC, in turn, provides an independent and protective running environment for the DMPS, which improves its operating efficiency (*28*). Specifically, the DMPS contains three modules: (i) signal convertor, which can dynamically receive and convert the fluctuant bioinformation (stimulus, i.e., extracellular molecules) to a fluctuant DNA analog signal for downstream molecular computation; (ii) fluctuation filter, which is composed of four incoherent FFLs and a threshold gate to determine whether the concentration of DNA signal exceeds the designated threshold, cut off the conduction when concentration of DNA signal falls below the threshold (weak noise), and conduct downstream pathway when concentration of DNA signal exceeds the threshold (meaningful stimulus); and (iii) intensity accumulator, which can accumulate dynamic signal filtered by the fluctuation filter via molecular catalysis–based recording. The DNA nanopores (NPs) embedded in the membrane of AC allow stimulus diffusion driven by osmotic pressure. By constructing a mixed cell community, the DMPS-powered ACs (DMPS-ACs) can dynamically sense, analyze, and process the meaningful stimulus from the environment or released by NCs instead of weak noise. We also showed that this NC-like dynamic information processing can be implemented in a blood vessel mimic. To the best of our knowledge, DMPS-AC is the smallest synthetic artificial system yet having dynamic bioinformation processing ability in a biological environment. The network topology–directed design strategy may pave the way for more bionic systems with dynamic functions or behaviors, which will deepen our understanding toward the network dynamics in biological systems.

[1]Molecular Science and Biomedicine Laboratory (MBL), State Key Laboratory of Chemo/Biosensing and Chemometrics, College of Chemistry and Chemical Engineering, College of Biology, Aptamer Engineering Center of Hunan Province, Hunan University, Changsha, Hunan 410082, China. [2]Shenzhen Research Institute, Hunan University, Shenzhen, Guangdong 518000, China. [3]Zhejiang Cancer Hospital, Hangzhou Institute of Medicine (HIM), Chinese Academy of Sciences, Hangzhou, Zhejiang 310022, China. [4]Institute of Molecular Medicine (IMM), Renji Hospital, Shanghai Jiao Tong University School of Medicine and College of Chemistry and Chemical Engineering, Shanghai Jiao Tong University, Shanghai 200240, China.
*Corresponding author. Email: lvyifan1990@hnu.edu.cn (Y.L.); tan@hnu.edu.cn (W.T.)

RESULTS

Network topology–directed design of DRN-based fluctuation filter

We first analogized the stimulus threshold of NCs that can distinguish meaningful stimulus from weak noise to a network topology called threshold gate, which asked whether the input value was bigger than the threshold value (Fig. 1A). A threshold gate is a key module in both electronic and molecular analog circuits, and it is prevalent in biological systems to drive various functions (4, 31, 32). Using DRN, a threshold gate can be easily implemented as shown in Fig. 1B. If the concentration of input strand I is lower than the threshold gate

(strand BC), then all strand I would be consumed, and no downstream pathway could be initiated. If the concentration of strand I is higher than BC, then BC would be consumed, and excess strand I can trigger downstream pathways. This traditional design is typical of DRN with a static input signal and irreversible consumption of components, which is incompatible with dynamic stimulus processing in a biological system (Fig. 1C) (29, 30, 33). We then focused on another kind of essential network topology harnessed by NCs for dynamic information process, FFLs, which link input to output with two paths (Fig. 1D) (17, 34). On the basis of whether the two paths connecting input and output have the same or different signs, FFLs are
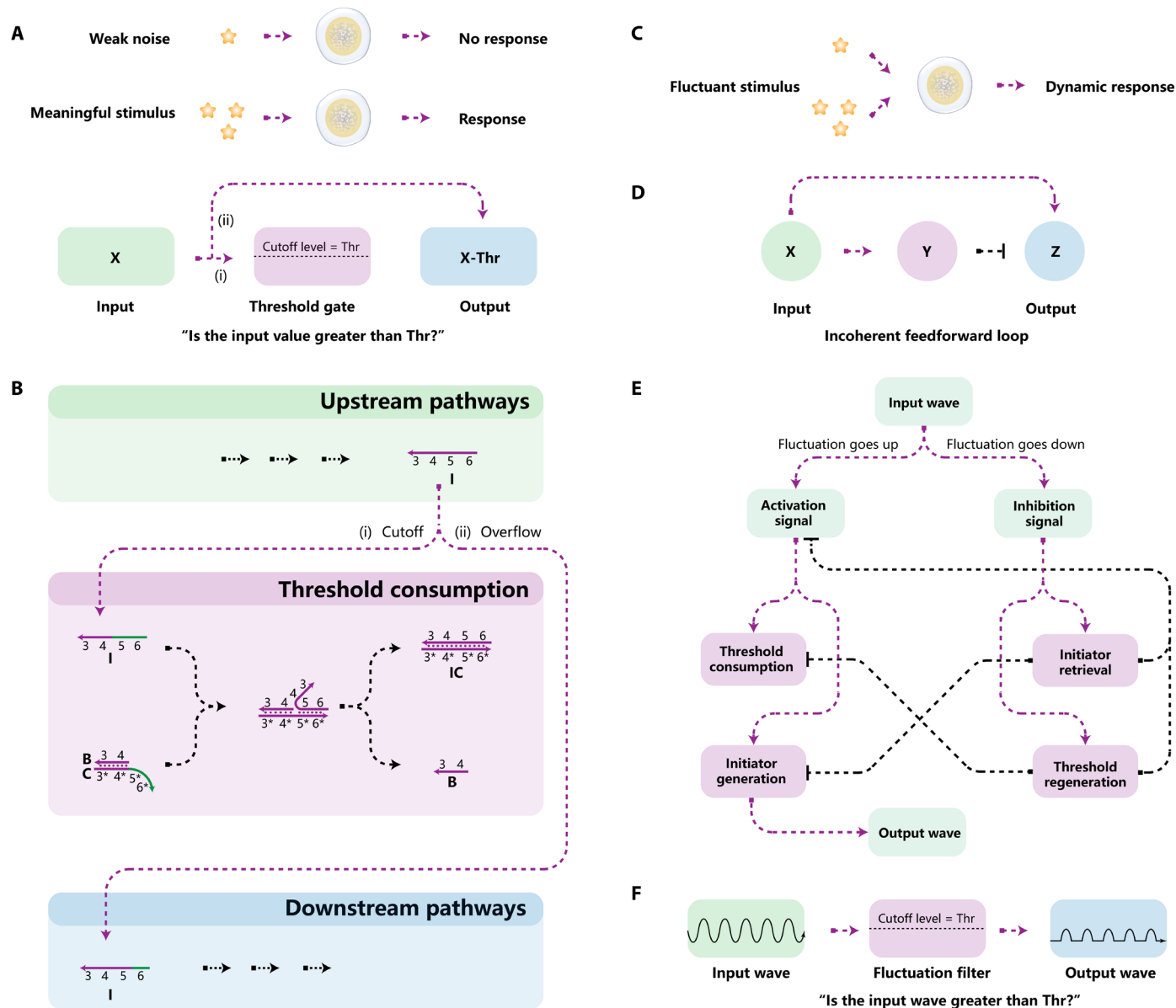
Fig. 1. Network topology–directed design of DRN-based fluctuation filter. (**A**) Flow diagram of a threshold gate simplified from stimulus threshold of NCs. (**B**) Static threshold gate design with a consumptive and irreversible threshold gate (BC). (**C**) NCs that can sense and response fluctuant stimulus. (**D**) The incoherent FFL used in this design with two pathways connecting input and output having the different signs. (**E**) Flow diagram of fluctuation filter integrating incoherent FFLs and threshold gates. Black dashed line denotes inhibition. (**F**) Flow diagram of network topology–directed fluctuation filter that can process a continuous and ever-changing input wave. Thr denotes threshold.

classified as either coherent or incoherent (fig. S1) (*35*). By integrating four incoherent FFLs with the threshold gate, we conceived a reconfigurable network topology in response to fluctuant input wave based on four submodules: threshold consumption, initiator generation, initiator retrieval, and threshold regeneration (Fig. 1, E and F). By implementing this network topology using DRN, a fluctuation

filter can be lastly built. When fluctuation goes up (stimulus increasing), input strand I can first consume threshold gate (strand BC) in the threshold tolerance state where strand I does not exceed BC. If strand I exceeds BC (Fig. 2 and fig. S2A), then strand D will be released as the output of fluctuation filter for initiating the downstream pathway. When fluctuation goes down (stimulus
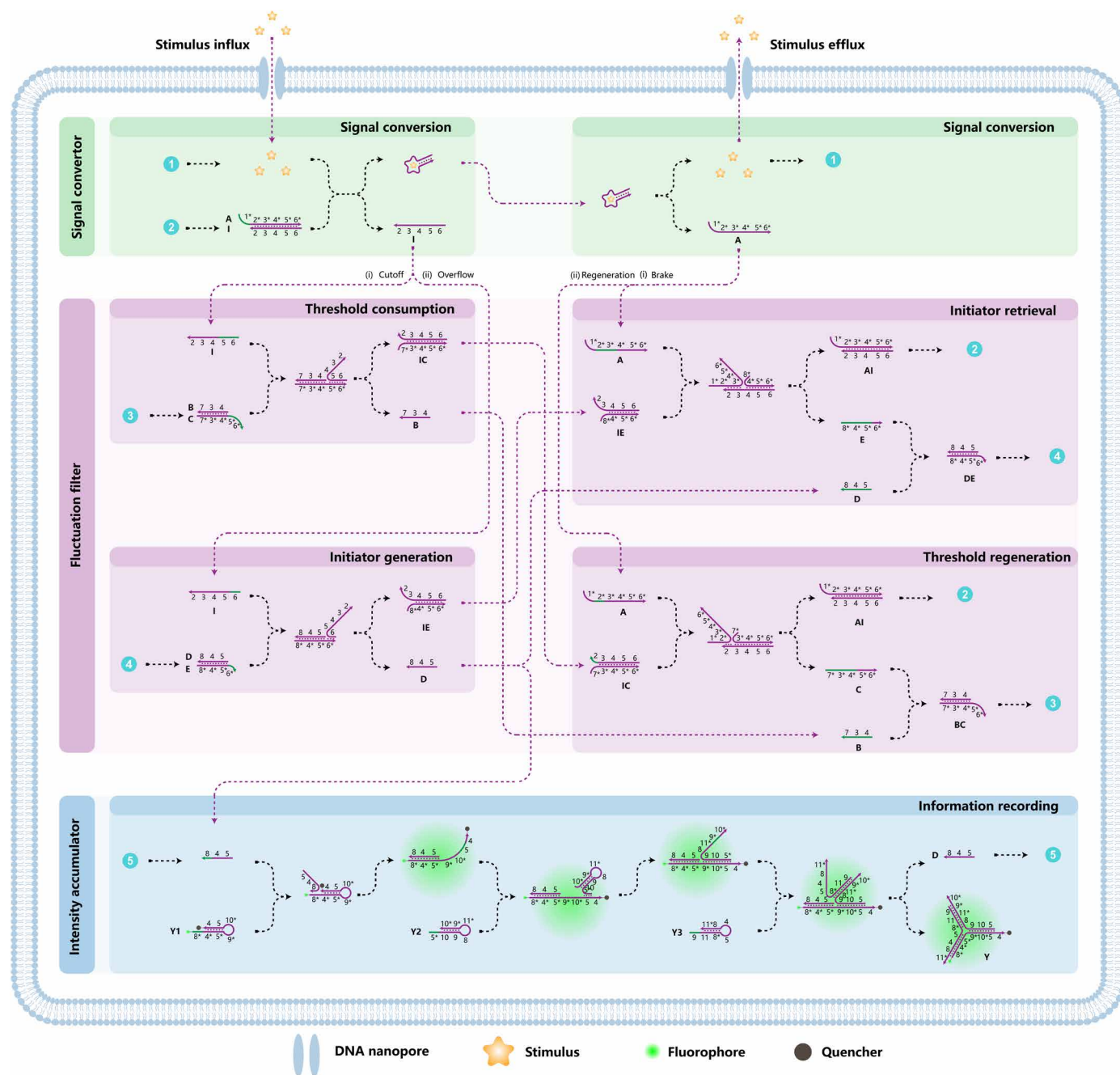
Fig. 2. Blueprint of DMPS-powered AC that has dynamic information processing ability. DMPS, as the mCPU of AC, contained three modules: a signal convertor for biosignal reception, a fluctuation filter for signal process, and an intensity accumulator for signal output and storage. The extracellular fluctuation of stimuli will, in turn, cause intracellular fluctuation of stimuli through influx or efflux driven by osmotic pressure. The fluctuant stimuli inside the AC are transduced into a fluctuant DNA analog via a signal convertor. The fluctuation filter can determine whether the fluctuant DNA analog signal exceeds or falls below a cutoff threshold value and only outputs the overflowing signal. This filtration process is continuous and autonomous, regardless of whether fluctuation goes up or down. The filtered signal can be recorded through the intensity accumulator and can be lastly reported by fluorescence output.

decreasing), released initiator will first be retrieved in the threshold-exceeded state to stop the initiator generation step and regenerate DE, and the consumed BC will then regenerate in threshold tolerance state to replenish threshold gate (Fig. 2 and fig. S2B). Meanwhile, both initiator retrieval and threshold regeneration steps can produce complex AI to replenish previously consumed AI (Figs. 1E and 2). We assessed the performance of the fluctuation filter by simulating random parameters in silico and confirmed that our fluctuation filter can analyze and filter dynamic information flow, with integrated FFLs and threshold gate acting as the source of dynamic filtering (figs. S3 to S6).

Construction and operation of DMPS

To receive and convert the fluctuant extracellular signal into dynamic DNA analog signal in DRN, a signal convertor was built as the fluctuation filter's upstream pathway. To accumulate the filtered signal, an intensity accumulator was built as the fluctuation filter's downstream pathway. The whole system, termed DMPS, was shown in Fig. 2. As a proof of concept, we chose a very common extracellular stimulus, K^+, as the model stimulus to verify the operation of the DMPS. Extracellular K^+ regulates cellular osmolality, cellular environmental homeostasis, and membrane potential. An abnormally fluctuant concentration of potassium ion above the maximal background concentration (extracellular 5 mM K^+) can cause neurological disorder, diabetes, kidney failure, heart disorder, and various cancers (36, 37). The K^+-specific signal convertor was based on G-quadruplex–mediated transduction, in which a fluctuating concentration of K^+

could be converted into a fluctuating concentration of strand I released from complex AI (fig. S7A). We here mimicked the K^+ fluctuation by alternately adding K^+ and 18-crown-6-ether (CE), a strong chelator of K^+, at the ratio of 1:1. When the concentration of K^+ increased, strand I was released to trigger following DRNs (Fig. 3A, fig. S7B, and sequences in table S1), while decreased K^+ allowed released strand A to hybridize with single-stranded DNA I (ssDNA I) to regain AI (Fig. 3B). To further verify the recovery of AI, quenched duplex AI assembled from FAM (carboxyfluorescein)-labeled A (FAM-A) and BHQ1 (Black Hole Quencher1)-labeled I (BHQ1-I) was alternately incubated with K^+ and CE to measure the fluorescence kinetics. Quenched AI could release FAM-A and BHQ1-I when incubated with K^+. FAM-A and BHQ1-I could also hybridize to retrieve quenched AI when CE chelated K^+ in buffer solution (fig. S8). Recoverable quenched AI could also execute the next release-retrieval cycle, allowing continued processing of dynamic stimulus fluctuation.

Then, we investigated the operation of the fluctuation filter. Polyacrylamide gel electrophoresis (PAGE) showed the consumption of threshold gate (BC) to generate IC and B with no consumption of DE when the concentration of I was no greater than the cutoff value of BC (lane 10 in Fig. 3C). DE would be consumed to generate initiator strands D and IE after the exhaustion of BC when the concentration of I exceeded the cutoff value of BC (lane 11 in Fig. 3C). The reaction occurred because the toehold of BC (5*6* domain) was longer than that of DE (6* domain), causing a faster reaction rate of BC by two orders of magnitude (29). The thermodynamic stability
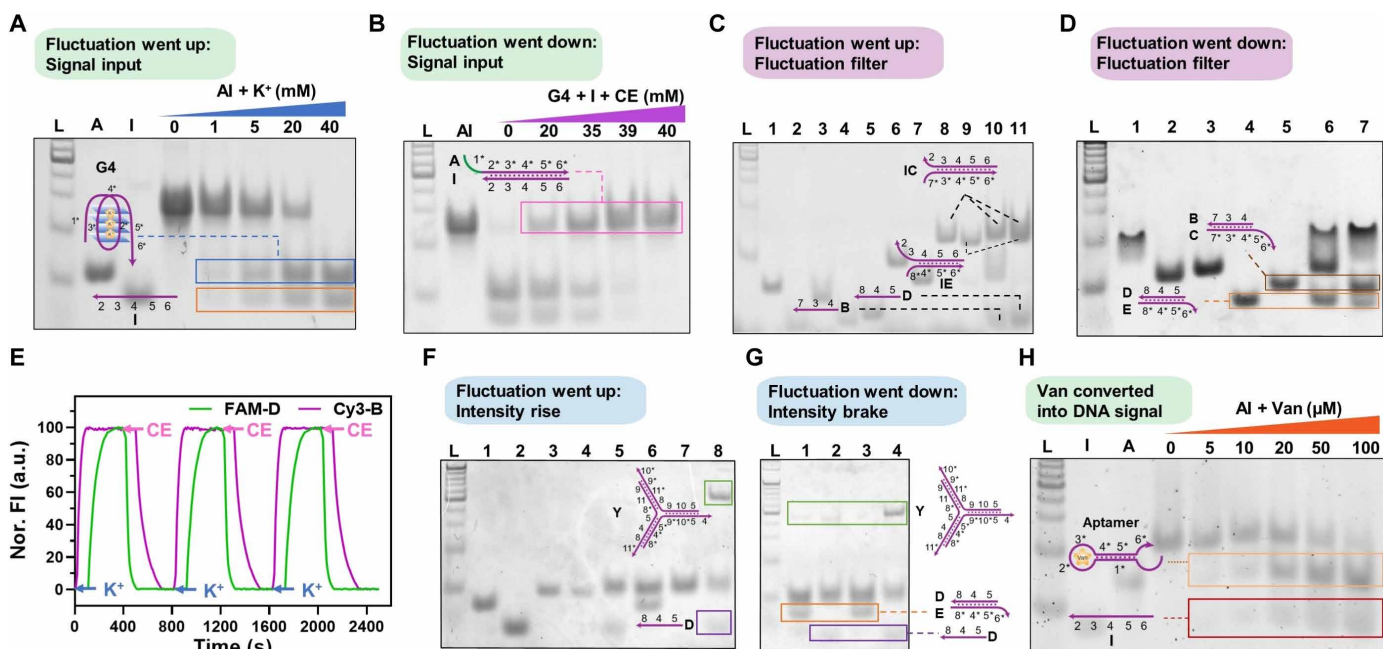
Fig. 3. Construction and operation of DMPS. (**A**) PAGE analysis of K^+-specific AI treated with different concentrations of K^+. G4, G-quadruplex. (**B**) PAGE analysis of K^+-specific AI (in the presence of initial 40 mM K^+) treated with different concentrations of CE. (**C**) PAGE analysis of fluctuation filter–controlled reaction pathways. Lanes 1 to 5: I, B, C, D, and E; lanes 6 to 9: BC, DE, IC, and IE; lanes 10: BC + DE + 1 equivalent. I (initial I, below cutoff value); and lane 11: BC + DE + 2 equivalent. I (including overflowing I). (**D**) PAGE analysis of fluctuation filter–controlled reaction pathways. Lanes 1 to 5: AI, IE, IC, DE, and BC; lane 6: IC, IE, B, and D incubated with 1 equivalent. A (initial A); and lane 7: IC, IE, B, and D incubated with 2 equivalent. A (including overflowing A). (**E**) A total of 200 nM quenched duplex BC and 200 nM quenched duplex DE with 400 nM AI were alternately incubated with 40 mM K^+ and 40 mM CE to test the fluorescence kinetics. a.u., arbitrary units. (**F**) PAGE analysis of CHA driven by strand D. Lanes 1 to 5: DE, D, Y1, Y1 + Y2, and D + Y1 + Y2; lane 6: DE + Y1 + Y2 + Y3; lane 7: Y1 + Y2 + Y3; and lane 8: D + Y1 + Y2 + Y3. (**G**) PAGE analysis of braking CHA reaction via strand E. Lane 1: 2-min CHA reaction (Y1 + Y2 + Y3 + D) and then incubated with 1 equivalent. E for 2 min; lane 2: 2-min CHA reaction; lane 3: Y1 + Y2 + Y3 + D + E simultaneously; and lane 4: CHA reaction for 10 min. (**H**) PAGE analysis of Van-specific AI treated with different concentrations of Van. L denotes 20–base pair (bp) DNA ladder.

of BC's reactive product was also higher because IC had a longer double-stranded DNA (dsDNA) domain than that of IE. The molecular computation–based selective reactive pathways were also verified by preferential generation of Cy3-B and following emergence of FAM-D (fig. S9). When fluctuation went down, strand A was released and first invaded by strand IE to gain AI and strand E, which could consume initiator strand D to brake downstream pathways (lane 6 in Fig. 3D). Controlled by the kinetics, only overflowing A could invade IC and subsequent B to regenerate AI and BC (lane 7 in Fig. 3D). The fluorescence kinetics curve also indicated the sequential reactions: preferential consumption of FAM-D and later reduction of Cy3-B (fig. S10). To further examine whether the threshold gate (BC) and initiator generator (DE) could be completely retrieved, 1 equivalent quenched duplex BC (assembled from Cy3-B and BHQ2-C) and DE (assembled from FAM-D and BHQ1-E) with two equivalent AI were alternately incubated with K^+ and CE to test the fluorescence kinetics (Fig. 3E). BC was preferentially consumed to release Cy3-B, and then overflowing K^+ activated the production of FAM-D. After CE was added to the system, FAM-D was first reduced because converted A preferentially reacted with IE and then overflowing A reacted with IC to consume Cy3-B. The fluorescence intensity (FI) of FAM-D and Cy3-B returned to the initial value after finishing a fluctuant cycle. The intensity curve had no apparent change after several fluctuant cycles, indicating the robustness and sustainability of the system.

We next investigated operations of the intensity accumulator module, which is based on a CHA (catalytic hairpin assembly) reaction catalyzed by initiator D released after filtration, contributing to either intensity rise or brake for recording the filtered signal. Such a catalysis-based design decoupled the reaction equilibrium between filter module and the accumulator module because the released catalyst D would not be consumed during the CHA reaction and only acted as an on-off switch in the accumulator module (38). Time-dependent leakage of the intensity accumulator was absolutely eliminated using rational mismatch design of hairpin sequences based on a previous report (39–41), and an optimized signal-background ratio (SBR) of about 10-fold was achieved (fig. S11). CHA product Y, which is a three-way junction, was formed by Y1, Y2, and Y3 in the presence of initiator D, while no reaction was observed in the presence of DE (Fig. 3F). When fluctuation went down, D was retrieved to gain DE to brake and then stop the successive generation of Y (lanes 1 to 4 in Fig. 3G and fig. S12). The K^+-specific DMPS was tested by combining all three modules, indicating successful fluctuation filtration and recording of filtered signal in an accumulating manner (fig. S12). Selectivity of DMPS was studied using 5 mM K^+ and 150 mM Na^+ individually as the input, and the fluorescence kinetic results showed that this response was K^+ specific (fig. S13). Then, we defined above 5 mM K^+ as the meaningful stimulus of our system and set the cutoff value of the threshold gate (BC) to see whether K^+-specific DMPS could filter out background K^+ noise and accumulate dynamic signal only when environmental K^+ exceeded 5 mM (37). When AI:BC was 4:1, there was an obvious fluorescence rise from 5 to 6 mM K^+ (fig. S14A). Therefore, we used AI:BC = 4:1 to conduct the following studies. The intensity of FAM-D indicated a rising tendency from zero when the system increased to 6 mM K^+ (fig. S14, B and D) and showed a fast drop to zero when the system decreased to 5 mM K^+ (fig. S14, C and D). These results proved that DMPS could filter out the K^+ background noise and respond to its meaningful value. To theoretically demonstrate the dynamic filtering mechanism of DMPS,

we constructed a quantitative thermodynamics model to determine the concentration boundary (text S1). By expressing the concentration of strand D as the function of input stimulus (K^+) based on the reaction equilibrium and strand conservation principle, we showed that the dynamic filtering was an inherent network property of the DMPS system. The computational filtering curve gave a turning point between 5 and 6 mM K^+, which was in correspondence to the experimental data (fig. S15).

Apart from K^+ as a fluctuant model of endogenous stimuli, we also challenged DMPS using the small-molecule drug, vancomycin (Van), as our next exogenous model (42), because an effective dose (about 7 to 14 μM) and the maximum tolerable dose (about 20 μM) of Van were so close so that it would be necessary to implement dynamic drug supervision (42, 43). PAGE results showed that a Van-specific signal convertor could convert concentration information of Van into a DNA analog signal through aptamer-mediated transduction (Fig. 3G and fig. S16A) (44). Similar to K^+-specific DMPS, a dynamic response of Van-specific DMPS could also be seen in fig. S16B. By defining above 14 mM Van as the meaningful stimulus, the cutoff value of Van-specific DMPS was determined when AI:BC was 6:1 (fig. S16C).

Construction and characterization of DNA NP–equipped AC

We then constructed an independent and protective operating environment for the DMPS by synthesizing DNA NP–equipped AC. We designed the cholesterol-modified DNA NP (tables S1 and S2) with a 2-nm channel using six strands (6NP) and characterized the assembly by agarose gel electrophoresis (AGE) and atomic force microscopy (AFM) imaging (Fig. 4A and fig. S17). This DNA NP can serve as an artificial transmembrane channel only permitting the transport of ions and small molecules, rather than enzymes, DNA, or proteins (28, 45, 46). We used the inverted microemulsion method to synthesize the ACs with ~26.5 μm in size (Fig. 4B) (47, 48). To verify the transport of K^+ and Van across the DNA NP–equipped AC membrane, K^+-specific AI (labeled by FAM and BHQ1) and Van-specific AI (labeled by Cy3 and BHQ2) were encapsulated into ACs to detect K^+ and Van. Confocal imaging indicated that only DNA NP–equipped ACs showed green or yellow fluorescence after K^+ or Van was added (Fig. 4C). These results proved that K^+ and Van could diffuse into DNA NP–equipped AC for further conversion into DNA analog signal.

After validating the transport of K^+ and Van, we investigated the structural stability of ACs in biological environment. First, we determined the isosmotic inner solution of AC to avoid rupture during storage and under physiological conditions (285 to 305 mOsm/kg of H_2O) (fig. S18). Second, we tested the stability of DNA NP–equipped AC in 10% fetal bovine serum (FBS) at 37°C. The DNA NP showed only slight degradation after 24 hours via PAGE analysis (fig. S19A). The fluorescence of Cy5-labeled DNA NP on AC did not become weaker after 24 hours of incubation (fig. S19B).

The DMPS was then built as the mCPU of AC for receiving and processing extracellular bioinformation (Fig. 4D). The stability of DMPS-AC was tested under cell culture conditions (Fig. 4, E and F). DMPS-AC still showed about 10-fold SBR (comparable to that under buffer condition) after 24-hour incubation in 10% FBS at 37°C, while free DMPS lost discriminative ability after 1-hour incubation (onefold SBR) (Fig. 4F). This result highlighted the importance of a protective running environment for our DRN-based mCPU. The reaction rate of DMPS in AC was about twofold faster than that of DMPS under buffer condition, even if SBRs, after reaching equilibrium, were similar (Fig. 4, G and H). Such a network acceleration
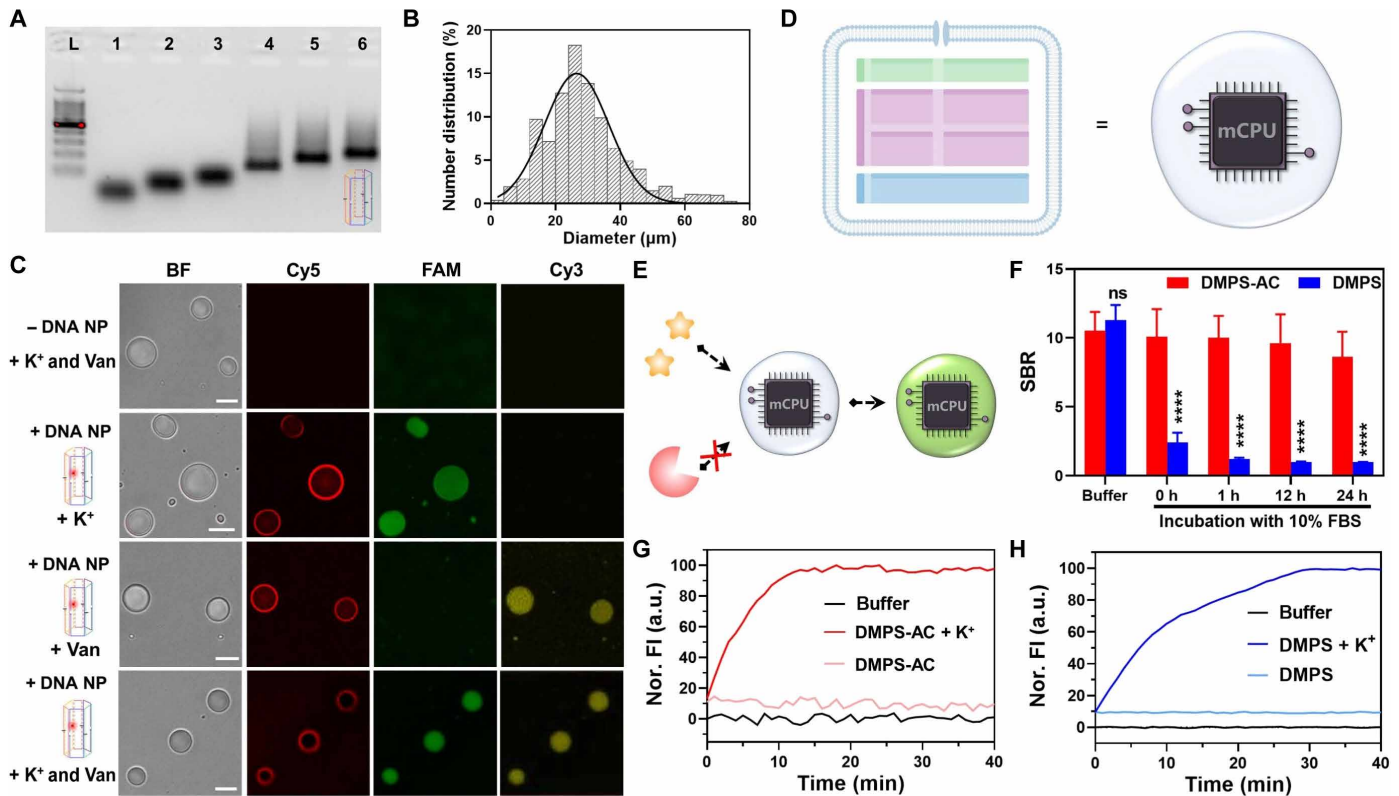
Fig. 4. Construction of DNA NP–anchored AC. (**A**) AGE analysis of stepwise assembly of DNA NP. Lane L, 100-bp DNA ladder; lanes 1 to 6, self-assembly of corresponding numbers of ssDNA building blocks. (**B**) Statistical analysis of size distribution from more than 200 ACs in microscopic imaging. (**C**) Fluorescence imaging of quenched dsDNA AI-embedded (K$^+$-responsive AI assembled from FAM-A with BHQ1-I; Van-responsive AI assembled from Cy3-A with BHQ2-I) ACs with or without Cy5-NP after 40 mM K$^+$ or 100 μM Van was added. Scale bars, 20 μm. (**D**) Scheme illustrating DMPS could be regarded as mCPU to power AC. (**E**) Scheme illustrating AC-mediated protection of inner DNA molecules from nuclease-mediated degradation owing to the limited size of DNA NP. (**F**) SBR analysis when DMPS-AC and free DMPS were treated with 40 mM K$^+$ at room temperature for 1 hour of kinetic scanning after incubation with 10% FBS or buffer at 37°C for different times, respectively. All data are means ± SD, $n = 3$. ****$P < 0.0001$; ns means no significant difference [two-way analysis of variance (ANOVA)]. (**G**) Fluorescence kinetics of DMPS-AC incubated with 40 mM K$^+$ in buffer. (**H**) Fluorescence kinetics of free DMPS incubated with 40 mM K$^+$ in buffer.

may result from the increased specific surface area caused by cell-sized confinement, because it has been reported that the surface effect of lipid membrane can accelerate encapsulated reactions (*49–51*). To verify this hypothesis, we mixed DMPS with different numbers of empty ACs and observed accelerating running speed, which indicated that the acceleration was positively related to the surface area of ACs (fig. S20). Besides, the effect of ion strengths on the running speed of DMPS-AC was also tested (fig. S21).

The information processing inside a DMPS-AC was formulated by computationally establishing a kinetic model. A set of differential equations following the kinetic profile was formulated and provided in text S2 (*52, 53*). To test the feasibility of this model, we designed and assembled another two DNA NPs (8NP and 4NP) with different channel sizes (fig. S22, A to D, and table S4). The influx kinetics of stimuli into the three-NP–anchored ACs was estimated by Fick's law (text S2 and fig. S22E) (*54, 55*). The set of rate constants acquired by fitting the time-dependent concentration changes of species in DMPS was given in table S5. By using this set of rate constants, the time-dependent influx of stimuli and concentration changes of network species were computationally estimated, which were corresponding to the experimental data (fig. S23). Because all three NPs showed fast stimulus influx kinetics, next, we still chose 6NP as the model to construct DMPS-AC.

Dynamic information processing of mCPU-powered AC

After constructing mCPU-powered AC, we further asked whether this artificial system could automatically and continuously process external fluctuant information (Fig. 5A). To address this question, we herein implemented two K$^+$ fluctuation models, alternating concentrations between 10 and 5 mM K$^+$ (10-5 model) and alternating concentrations between 6 and 5 mM K$^+$ (6-5 model), to survey the processing behavior of DMPS-AC as these models mimicked clinical values of severe hyperkalemia and moderate hyperkalemia. As shown in Fig. 5B, fluorescence imaging kinetics showed that 10 mM K$^+$ caused a surge of fluorescence (0 to 3 min), while treatment of 5 mM CE braked the rise in fluorescence (3 to 6 min) because the converted DNA signal was filtered out by the threshold gate when K$^+$ concentration fell below 5 mM. Then, 5 mM K$^+$ and 5 mM CE were added alternately and led to rise and brake in fluorescence accordingly. Compared with a fast emergence (3 min) of obvious fluorescence in the 10-5 model (Fig. 5, B and C), no apparent signal emerged until 40 min in the 6-5 model (Fig. 5, D and E), a sign that extreme fluctuation above threshold could cause fast signal accumulation in a short time, whereas it would take a long time for mild fluctuation to do it. The two distinct responsive speeds indicated our DMPS-powered AC could process meaningful fluctuations of different levels. Besides, background noise fluctuation from 3 to 5 mM K$^+$,

steady concentration below the cutoff value (5 mM K^+), and only a few meaningful fluctuations did not contribute to apparent fluorescence signal (fig. S24). These results clarified our artificial system could specifically process and discriminate different fluctuation situations of stimuli and output corresponding fluorescence results.

Similarly, Van-specific DMPS-AC was also constructed using Van-specific mCPU to power ACs. The extracellular fluctuation of Van was achieved by continuously diluting the extracellular environment for the absence of any available chelator of Van. A fluorescence signal emerged at 5 min and was saturated at 100 min when alternating between 30 and 14 μM Van (30-14 model), while a fluorescence signal was observed at 100 min when alternating between 20 and 14 μM Van (20-14 model) (Fig. 5, F and I). Similar to fluctuant K^+, neither background noise below cutoff value nor a transient overflowing drug concentration caused observable fluorescence (fig. S25). These results supported that the DMPS-AC was feasible and versatile for precise, continuous, and dynamic bioinformation processing.

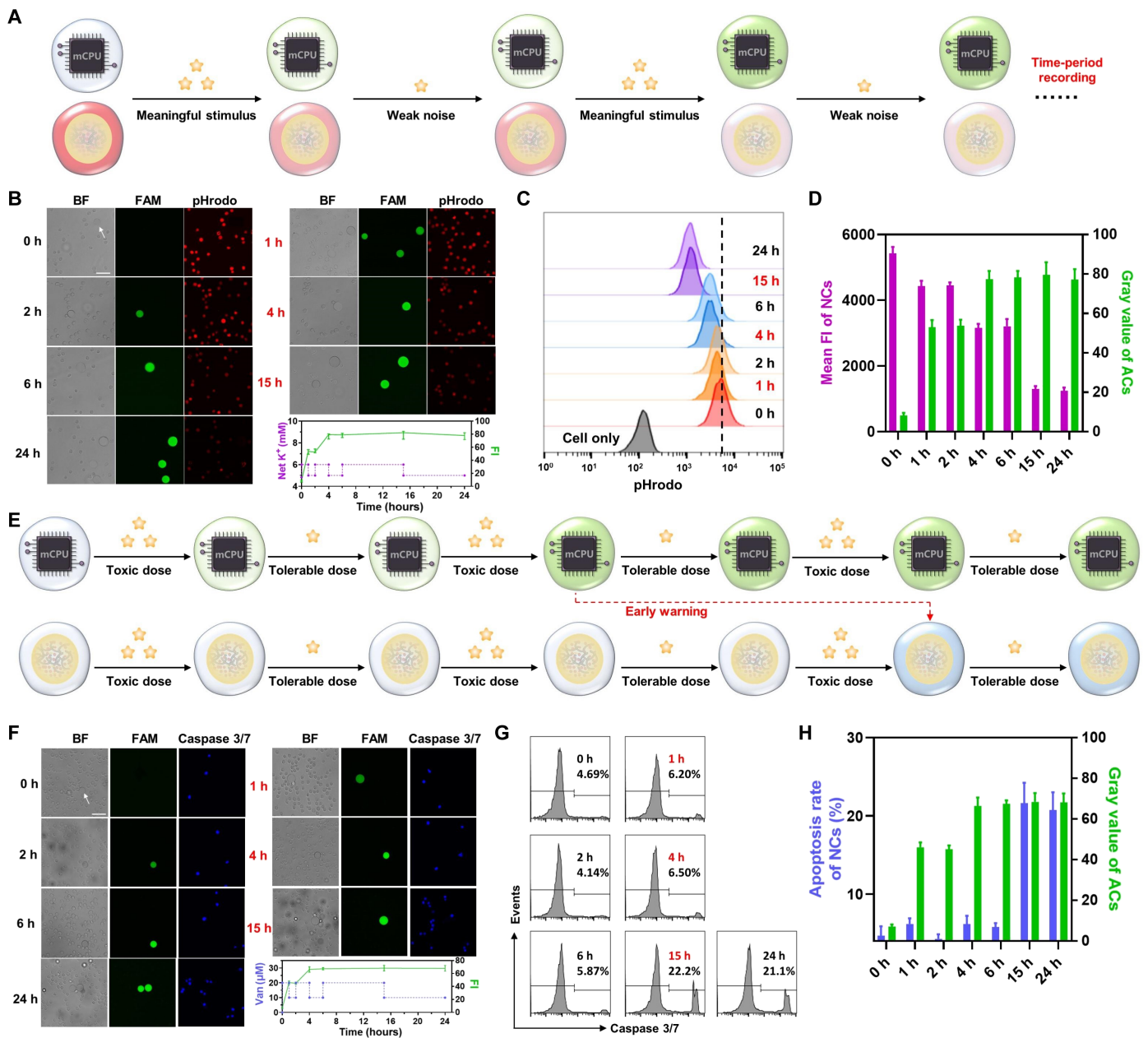## Response of mCPU-powered AC in live cell bioenvironments

After confirming the dynamic information processing ability of DMPS-AC, we constructed a mixed cell community using both DMPS-ACs and NCs to study their response to the dynamic stimuli under physiological condition (Fig. 6A). After verifying the biocompatibility of mCPU-powered ACs against live CCRF-CEM cells (fig. S26), we set the 6-5 model in complete RPMI 1640 medium at 37°C (Fig. 6B, purple dotted line). Because a high K^+ concentration can cause alkalization of NCs (56, 57), we used a pHrodo probe to monitor the pH changes of NCs. DMPS-ACs and NCs showed similar response to continuous fluctuation of K^+. The fluorescence of DMPS-ACs rose only when

K^+ exceeded the cutoff value, otherwise remaining fixed (Fig. 6A). Note that the fluorescence of DMPS-ACs would reach saturation when CHA substrates were exhausted. For NCs, the weaker red fluorescence of pHrodo probe indicated the higher pH value. When K^+ reached a meaningful stimulus level, i.e., exceeded the cutoff value (0 to 1, 2 to 4, 4 to 6, and 6 to 15 hours), the intracellular pH value of NCs increased because the influx of K^+ with overflowing concentration caused intracellular H^+ efflux to adapt to the osmolality change (Fig. 6, B to D, and fig. S27). However, even if K^+ fell into the background level (1 to 2, 4 to 6, and 15 to 24 hours), the intracellular pH value of NCs did not return to its initial basis (Fig. 6, B to D). These results revealed that DMPS-AC and NC had synchronous response to extracellular stimulus fluctuation based on their DRN or biological reaction network and indicated that DMPS-AC could effectively accumulate and record the meaningful signals during a monitoring period.

Successful dynamic information processing was also observed in the Van-specific model when the cell community encountered abnormal fluctuation of Van. Van fluctuation above the cutoff value (tolerable dose) could be sensed and processed by NCs, which caused irreversibly accumulated apoptosis (toxic dose). Van-specific DMPS-AC worked well by filtering out the tolerable Van dose and accumulating the overflowing toxic dose. Here, Van-specific DMPS-AC could act as an "alarm" to give an early warning for the NC's apoptosis event (Fig. 6E). The accumulated signal of Van-specific DMPS-AC became obvious within 2 hours and reached saturation at 4 hours, while the apparent apoptosis event of NC could not be observed until 15 hours (Fig. 6, F to H). This can be attributed to the fact that DMPS-AC could quickly receive and process fluctuant Van information, while NC needs to implement a series of signal transduction
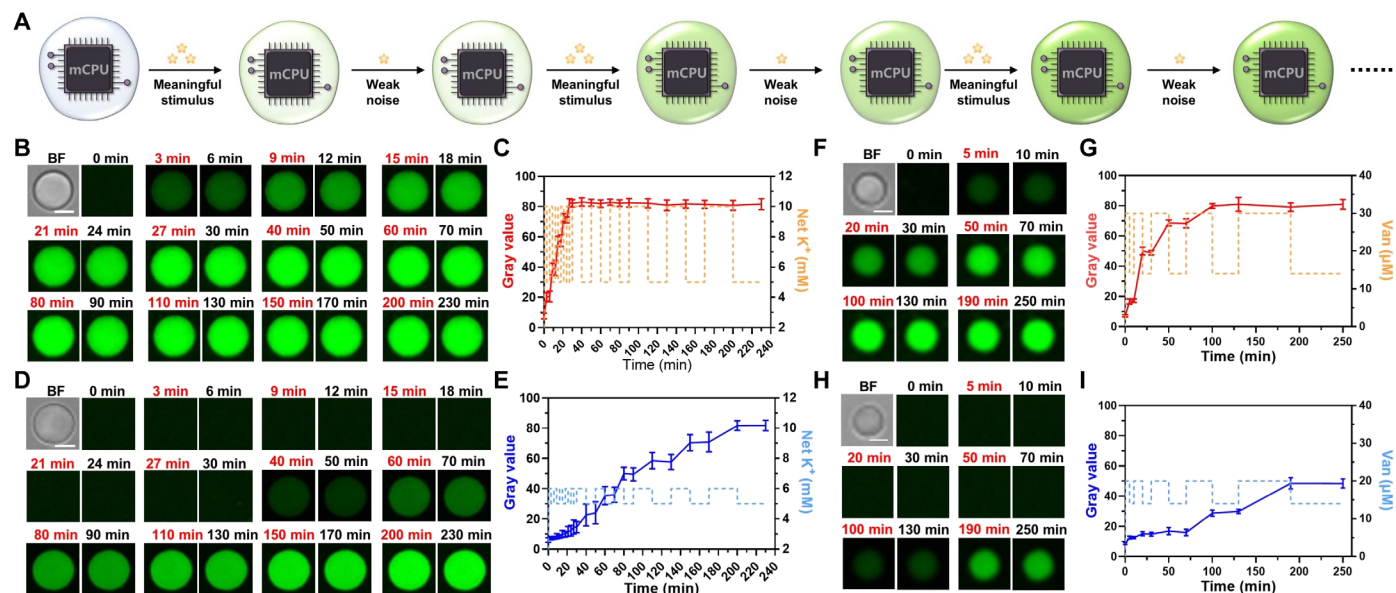
Fig. 5. Dynamic information processing of DMPS-AC responded to fluctuant concentrations of K^+ or Van. (**A**) Scheme illustrating information processing of DMPS-AC responded to dynamic extracellular stimuli. (**B**) Fluorescence imaging kinetics of DMPS-AC incubated with alternating concentrations of 10 or 5 mM K^+. (**C**) FI analysis and K^+ treatment of (B). (**D**) Fluorescence imaging kinetics of DMPS-AC incubated with alternating concentrations of 6 or 5 mM K^+. (**E**) FI analysis and K^+ treatment of (D). (**F**) Fluorescence imaging kinetics of DMPS-AC incubated with alternating concentrations of 30 or 14 μM Van. (**G**) FI analysis and Van treatment of (F). (**H**) Fluorescence imaging kinetics of DMPS-AC incubated with alternating concentrations of 20 or 14 μM Van. (**I**) FI analysis and Van treatment of (H). All data are means ± SD (n = 3) in (C), (G), (E), and (I). Scale bars, 20 μm. All concentrations are more than cutoff value from black time points to red time points, and all concentrations are less than cutoff value from red time points to black time points in (B), (D), (F), and (H). BF, bright field.

Fig. 6. mCPU-powered AC responded to extracellular fluctuant stimuli under live-cell environments. (**A**) Scheme illustrating the fluorescence response of DMPS-AC and NC to fluctuant stimuli (K$^+$ concentrations). (**B**) The mixture of DMPS-ACs and NCs (1:20) was incubated with fluctuant concentrations of 6 or 5 mM K$^+$. FAM channel indicates signal intensity of DMPS-AC. pHrodo indicates the pH value of NCs; stronger red signal denotes bigger pH value. (**C**) Flow cytometry analysis of NCs in (B). (**D**) Statistical analysis of (C). (**E**) Scheme illustrating the fluorescence response of DMPS-AC and NC to fluctuant stimuli (Van concentrations). (**F**) The mixture of DMPS-ACs and NCs (1:50) was incubated with fluctuant concentrations of 20 or 10 μM Van. FAM channel indicates signal intensity of DMPS-ACs. Blue caspase 3/7 channel indicates the apoptosis level of NCs; stronger blue signal denotes higher apoptosis. (**G**) Flow cytometry analysis of NCs in (F). (**H**) Statistical analysis of (G). Rows denote DMPS-ACs of all control groups (0 hour) in (B) and (F). All data are means ± SD ($n = 3$) in (B), (D), (F), and (H). Scale bars, 50 μm.

pathways to execute apparent apoptosis. To eliminate the influence of toxic Van dose between 6 and 15 hours on the apoptosis, we set no fluctuation between 6 and 24 hours (tolerable dose) compared to the fluctuation model in Fig. 6F and found that NCs still showed apparent apoptosis at 15 hours (fig. S28, A to C), indicating that the programmed apoptosis of NCs at 15 hours was caused by toxic stimulus fluctuation in the first 4 hours. In contrast, there were no apoptotic events of NCs after incubation with tolerable dose for

24 hours (fig. S28D). These results suggested the application potential of DMPS-AC in early warning about delayed accumulating behaviors of NCs, e.g., apoptosis, caused by toxic stimulus fluctuation.

Because cells do not live in isolation and their survival also depends on receiving and processing information between themselves, we subsequently investigated whether DMPS-AC could also process and record the dynamic information released from NC. We used 5 μM amphotericin B and 10 μM ouabain as the trigger to stimulate

CEM cells to pump out K^+ (Fig. 7A) (58). The excreted K^+ caused K^+ fluctuation in extracellular microenvironment, which was sensed and processed by DMPS-AC. An apparent accumulation of fluorescence in DMPS-AC occurred within 15 to 30 min because the fluctuant K^+ concentration in extracellular microenvironment exceeded the cutoff value of DMPS (Fig. 7, B and C). Then, we reduced K^+ concentration by manually adding CE to the mixed cell community at 30 min. As a result, fluorescence accumulation braked within 30 to 90 min because K^+ concentration fell below the cutoff value of DMPS under chelation (Fig. 7, B and C). Meanwhile, NCs continuously pumped out K^+, and after 90 min, the excreted K^+ again exceeded the cutoff value of DMPS, leading to a second round of signal accumulation. This result illustrated both cellular communication and information processing ability of DMPS-AC and demonstrated the potential of DMPS-ACs to in situ analyze and record physiological changes of NCs in biological microenvironment.

As a preliminary exploration of further work scene of DMPS-AC, a blood vessel–mimic circulation system was constructed using capillaries and peristaltic pump with circulating mixture of DMPS-ACs and NCs (Fig. 7D and fig. S29) (59). K^+ and CE were manually and alternatively added into the circulation system to implement a fluctuating environment, while the mixture of DMPS-ACs and NCs was pipetted out at different time points to measure the responding results. The fluorescence signal of DMPS-AC and alkalization of NC both became stronger when extracellular K^+ exceeded the cutoff value (0 to 1 and 2 to 3 hours, Fig. 7, E and F). Accordingly, both fluorescence signal of DMPS-AC and alkalization of NC remained changeless when extracellular K^+ fell below the cutoff value (1 to 2 hours). The circulation time of DMPS-AC in the blood vessel–mimic circulation system was tested. The relative number of DMPS-ACs slowly decreased to 88% at 12 hours and 71% at 24 hours (fig. S30). These results demonstrated the potential of DMPS-AC as a cell-sized

bioinformation processing device in vascular system with programmed functions.

DISCUSSION

In summary, to the best of our knowledge, we have proposed the smallest prototype artificial system to process fluctuant bioinformation in biological environment using DMPS as the mCPU to power synthetic ACs. Inspired by biological network topology, DMPS allows ACs to dynamically filter meaningful stimuli from background noise and accumulate overflowing signal. By constructing a mixed cell community, DMPS-AC and NCs were observed to have synchronous response to fluctuant extracellular stimuli under physiological condition and in a blood vessel–mimic circulation system. In addition, dynamic bioinformation released by NCs can also be received and processed by DMPS-ACs, indicating the communication ability of DMPS as the mCPU of ACs. This work achieved the evolution of AC functions through network topology directed DRN design and provided a new paradigm for understanding the mechanisms controlling biological reaction networks.

DMPS-AC is still in its early developing stage, and the functions we realized in this work only include continuous signal conversion, filtration, and accumulation. Future studies may include integrating more processing modules for biomedical applications in response to dynamic stimuli and improving the stability of the ACs for prolonged blood circulation time. A possible strategy to stabilize the structure of AC is to build artificial cytoskeleton inside or outside the AC membrane to reduce rupture during long-term circulation (60). For the equipped DNA NP and encapsulated DNA network, nuclease-resistant nonnatural nucleic acids such as L-DNA can be used to enhance system robustness. In the current design, the signal convertor and fluctuation filter theoretically have no limit on operation
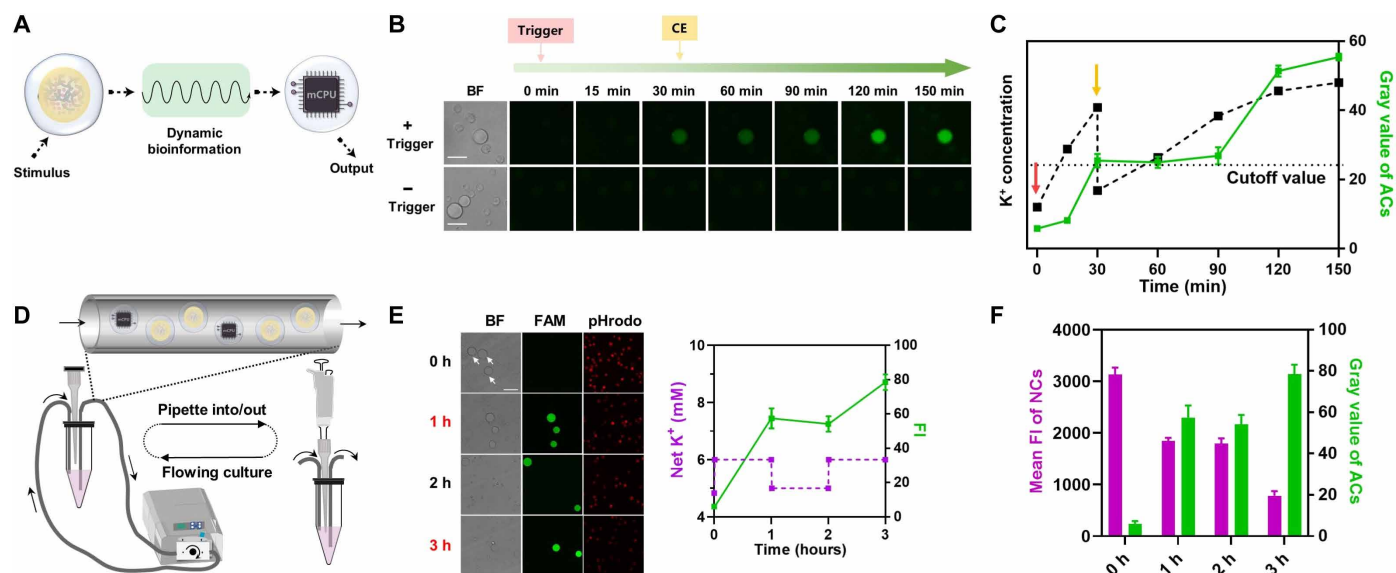
Fig. 7. Response of mCPU-powered AC with NC and in blood vessel–mimic circulation system. (**A**) Scheme illustrating stimulated NC released K^+ to DMPS-AC. (**B**) Representative fluorescence kinetic imaging of DMPS-AC and NC in RPMI 1640 medium by adding trigger, 5 μM amphotericin B, and 10 μM ouabain. (**C**) Quantification analysis of FAM intensity and proposed K^+ concentration's tendency of the group treated with trigger. Red arrow denotes adding trigger, and yellow arrow denotes adding 1 mM CE to reduce the concentration of K^+ in (B). (**D**) Construction of circulation system by mimicking blood vessels and controlling the concentrations of K^+ for diagnosis and readout of recorded results of NC and DMPS-AC. (**E**) Fluorescence kinetic imaging of the mixture of NCs and DMPS-ACs pipetted from (D). (**F**) Statistical analysis of (E). All data are means ± SD ($n = 3$) in (C), (E), and (F). Scale bars, 50 μm.

time, but the intensity accumulator, however, can still become exhausted. A simple way to extend the operation time is to encapsulate more CHA substrate strands as required so that the signal reporter can have more fuels. Another possible solution is to design enzyme-mediated replication and amplification systems fueled by external molecules such as adenosine 5′-triphosphate to generate reporter strands. Dissipative strategy may also be a solution to achieve longer operation time. As reported recently by Willner and colleagues (61) and Ricci and colleagues (62), energy-dissipating reactions have been integrated with DNA strand–displacement reactions to generate some unique properties, for example, temporal reactivation of DNA systems. By integrating with these strategies, we look forward to more functional DMPS modules with longer operation time and less external fuel dependence. We believe that the ability of dynamic information processing may inspire more sophisticated molecular designs for autonomous biological functions of artificial system. The mCPU design proposed in this work may also have application prospects in intelligent molecular diagnosis and in situ bioinformation analysis.

MATERIALS AND METHODS

General materials and apparatus
All small-molecule chemicals used in this study were purchased from Energy Chemical, unless otherwise described. All oligonucleotides in table S1 were purchased from Hippo Biotech and dissolved in double-distilled H_2O from Milli-Q. pHrodo red and caspase 3/7 probes were obtained from Thermo Fisher Scientific. Super GelRed and agarose were obtained from US Everbright Inc. Stains-all was purchased from Sangon Biotech. FBS was purchased from Sijiqing, Zhejiang, China. Polymerase chain reaction tubes were purchased from NEST Biotechnology. Osmotic pressure was measured using an osmometer from YASN Co. Other reagents and materials were obtained from Sigma-Aldrich, unless otherwise specified.

AGE and PAGE
To study the assembly and stability of three DNA NPs (8NP, 6NP, and 4NP, sequences in table S1), after nanoassemblies were executed as described in table S2, 3% AGE was carried out in 1× TBE/Mg [90 mM tris, 9 mM boric acid, 1 mM EDTA, and 5 mM Mg^{2+} (pH 8.0)] at 110 V for 30 to 60 min. To investigate the DRN, corresponding treated samples were run with 10% native PAGE in 1× TBE/Mg at 110 V for 60 to 90 min. AGE gels were stained with Super GelRed. PAGE gels were stained with Stains-all. All gels were imaged using the Bio-Rad ChemiDoc XRS System or a ChampChemi imaging and analysis system (Sage Creation, Beijing, China).

Fluorescence kinetics assays
All fluorescence kinetics assays were finished with a Synergy 2 Multi-Mode Microplate Reader (BioTek). To test DNA strand–mediated reactions without AC, 100 µl of 200 nM strands were tested at room temperature for 1 hour until equilibrium, unless otherwise specified. To test DMPS-AC, 10^5 ACs of 30 µl were tested in buffer [Dulbecco's phosphate-buffered saline (DPBS) chelated with 4.2 mM CE and supplemented with 5 mM $MgCl_2$] or in 10% FBS.

AFM imaging
Initially, 20 µl of 1× TBE/Mg was added on the surface of freshly cleaved mica for enhancing the adhesion of DNA samples. Afterward, 10 µl of 10 nM purified DNA NPs were deposited for 5 min to allow for adsorption. Last, the mica was rinsed with ultrapure water three times and dried in nitrogen atmosphere. AFM of samples was observed on a MultiMode 8 (Bioscope System, Bruker, USA) using Scan Assist mode in atmosphere.

Synthesis of AC
The procedures to synthesize giant vesicles and ACs were based on the inverted microemulsion method of water in oil with some modifications (47, 48, 63). Briefly, storage solution, 10 µl of 1-palmitoyl-2-oleoyl-sn-glycero-3-phosphocholine (POPC) (50 mg/ml) dissolved in $CHCl_3$, was first completely dried. Then, 1 ml of mineral oil was added to dissolve the lipid film, as 1.5-ml Eppendorf tube A, by incubating at 85°C until the undissolved POPC was no longer visible (about 20 to 40 min). Meanwhile, required DNA strands were dissolved in 280 mM sucrose with 5 mM Mg^{2+}, as inner solution in tube B. Tube C contained 500 µl of outer solution, consisting of DPBS with 5 mM Mg^{2+}, but without K^+ (chelated by 4.2 mM CE). A total of 20 µl of inner solution was pipetted into 400 µl of lipid-in-oil solution and then sonicated in a water bath for 30 to 60 min to form a water-in-oil emulsion. The emulsion was equilibrated at room temperature for 2 min and overlaid onto the interface solution of tube C, followed by 5 min of static incubation in a centrifuge. Giant vesicles were formed and pelleted by centrifugation at 5000g for 5 min. The bottom giant vesicles were then incubated with 200 nM DNA NP for 1 hour, followed by washing with DPBS (with 5 mM Mg^{2+} and without K^+) to store at 4°C.

Culture of NC and storage of AC
CEM cell line used in the study was purchased from American Type Culture Collection, Manassas, VA, USA. CEM cells were cultured in RPMI 1640 medium supplemented with 10% FBS, penicillin (100 U/ml), and streptomycin (0.1 mg/ml) at 37°C in 5% CO_2 atmosphere. Original complete RPMI 1640 medium has 4.83 mM K^+, and original DPBS has 4.16 mM K^+. To conveniently control the fluctuant concentrations of K^+, RPMI 1640 medium and DPBS used in the study were adjusted to 5 mM K^+. However, synthesized ACs were stored in DPBS without K^+ at 4°C.

Cytotoxicity assay
CEM cells (NCs; a total of 6×10^3) were plated in a 96-well plate, and then ACs of different ratios were added to incubate at 37°C for 24 hours. After that, cell mixtures were incubated with 10% Super Sensitive CCK-8 (Shanghai Shangbao Biotec) for about 1 hour. Then, the absorbance at 450 nm was collected using the Synergy 2 Multi-Mode Microplate Reader (BioTek) to determine the cell viability of NCs.

Microscope imaging and flow cytometry assays
To verify membrane anchoring of DNA NP and delivery of K^+ and Van, after 200 nM Cy5-labeled DNA NP were incubated with the prepared ACs (equipped with K^+-specific AI, FAM-A hybridized with BHQ1-I; and another Van-specific AI, Cy3-A hybridized with BHQ2-I), 40 mM K^+ or 100 µM Van was added and then subjected to imaging.

To investigate the stability of membrane anchoring of DNA NP, the DNA NP–anchored ACs were incubated in complete RPMI 1640 medium at 37°C for 24 hours and then washed for imaging. To execute imaging kinetics of DMPS-AC of K^+ model, K^+ and CE of high-concentration storage solution were added alternatively to control the fluctuation change of net K^+. To execute imaging kinetics of DMPS-AC of the drug model, Van of high-concentration storage solution was used to increase the drug concentration, and an extra

buffer was added to dilute the drug concentration because the volume of AC cannot be changed. To investigate the synchronous response of ACs and NCs (CEM cell line) when concentrations of extracellular K^+ or Van fluctuates, ACs and NCs were mixed at the ratio of 1:20 or 1:50 to incubate in complete RPMI 1640 medium at 37°C for designated time and designated fluctuation, respectively. Then pHrodo or caspase 3/7 probe was added, followed by imaging.

For the flowing circulation system, a closed-loop circulation was established by connecting a peristaltic pump and a 1.5-ml Eppendorf tube with polyvinyl chloride tubing to mimic the in vivo blood vessel and circulation system (Fig. 7D and fig. S29) (59). Experiments were conducted by mixing ACs and NCs at the ratio of 1:20 into a 1.5-ml tube containing 0.3 ml of RPMI 1640 medium, and circulation was kept at a speed of 5.2 ml/min for 3 hours. By inserting a 10-μl pipette tip, K^+ and CE could be added into the tube, and the cells were pipetted out of the system for imaging. For flow cytometry assays, CEM cells (NCs) were treated as previously described conditions in the fluorescence imaging assays, followed by staining and testing in DxP Athena (Cytek Biosciences Inc.).

Statistical analysis
Statistical data are means ± SD. n denotes three unless specifically declared. All statistical analysis was completed in GraphPad Prism 8 (La Jolla, CA, USA). Gray value in fluorescence imaging was determined using ImageJ software.

SUPPLEMENTARY MATERIALS
Supplementary material for this article is available at https://science.org/doi/10.1126/sciadv.abq0917

REFERENCES AND NOTES
1. M. Omidvar, J. Zdarta, S. B. Sigurdardottir, M. Pinelo, Mimicking natural strategies to create multi-environment enzymatic reactors: From natural cell compartments to artificial polyelectrolyte reactors. *Biotechnol. Adv.* **54**, 107798 (2021).
2. X. Wang, L. Tian, Y. Ren, Z. Zhao, H. Du, Z. Zhang, B. W. Drinkwater, S. Mann, X. Han, Chemical information exchange in organized protocells and natural cell assemblies with controllable spatial positions. *Small* **16**, e1906394 (2020).
3. D. Hiraoka, R. Aono, S. Hanada, E. Okumura, T. Kishimoto, Two new competing pathways establish the threshold for cyclin-b-cdk1 activation at the meiotic g2/m transition. *J. Cell Sci.* **129**, 3153–3166 (2016).
4. K. Rateitschak, O. Wolkenhauer, Thresholds in transient dynamics of signal transduction pathways. *J. Theor. Biol.* **264**, 334–346 (2010).
5. B. C. Buddingh, J. C. M. van Hest, Artificial cells: Synthetic compartments with life-like functionality and adaptivity. *Acc. Chem. Res.* **50**, 769–777 (2017).
6. A. Samanta, V. Sabatino, T. R. Ward, A. Walther, Functional and morphological adaptation in DNA protocells via signal processing prompted by artificial metalloenzymes. *Nat. Nanotechnol.* **15**, 914–921 (2020).
7. Y. Qiao, M. Li, R. Booth, S. Mann, Predatory behaviour in synthetic protocell communities. *Nat. Chem.* **9**, 110–119 (2017).
8. R. Lentini, N. Y. Martin, M. Forlin, L. Belmonte, J. Fontana, M. Cornella, L. Martini, S. Tamburini, W. E. Bentley, O. Jousson, S. S. Mansy, Two-way chemical communication between artificial and natural cells. *ACS Cent. Sci.* **3**, 117–123 (2017).
9. L. Rodriguez-Arco, M. Li, S. Mann, Phagocytosis-inspired behaviour in synthetic protocell communities of compartmentalized colloidal objects. *Nat. Mater.* **16**, 857–863 (2017).
10. T. Chakraborty, S. V. Wegner, Cell to cell signaling through light in artificial cell communities: Glowing predator lures prey. *ACS Nano* **15**, 9434–9444 (2021).
11. Z. Xu, T. Hueckel, W. T. M. Irvine, S. Sacanna, Transmembrane transport in inorganic colloidal cell-mimics. *Nature* **597**, 220–224 (2021).
12. S. Liu, Y. Zhang, M. Li, L. Xiong, Z. Zhang, X. Yang, X. He, K. Wang, J. Liu, S. Mann, Enzyme-mediated nitric oxide production in vasoactive erythrocyte membrane-enclosed coacervate protocells. *Nat. Chem.* **12**, 1165–1173 (2020).
13. P. Gobbo, L. Tian, B. Pavan Kumar, S. Turvey, M. Cattelan, A. J. Patil, M. Carraro, M. Bonchio, S. Mann, Catalytic processing in ruthenium-based polyoxometalate coacervate protocells. *Nat. Commun.* **11**, 41 (2020).
14. D. Clausznitzer, G. Micali, S. Neumann, V. Sourjik, R. G. Endres, Predicting chemical environments of bacteria from receptor signaling. *PLoS Comput. Biol.* **10**, e1003870 (2014).
15. H. J. Wagner, S. Kemmer, R. Engesser, J. Timmer, W. Weber, Biofunctionalized materials featuring feedforward and feedback circuits exemplified by the detection of botulinum toxin A. *Adv. Sci.* **6**, 1801320 (2019).
16. P. T. Ravindran, S. McFann, R. H. Thornton, J. E. Toettcher, A synthetic gene circuit for imaging-free detection of signaling pulses. *Cell Syst.* **13**, 131–142.e13 (2022).
17. O. Atay, A. Doncic, J. M. Skotheim, Switch-like transitions insulate network motifs to modularize biological networks. *Cell Syst.* **3**, 121–132 (2016).
18. T. M. Norman, N. D. Lord, J. Paulsson, R. Losick, Memory and modularity in cell-fate decision making. *Nature* **503**, 481–486 (2013).
19. S. Li, Q. Jiang, S. Liu, Y. Zhang, Y. Tian, C. Song, J. Wang, Y. Zou, G. J. Anderson, J. Y. Han, Y. Chang, Y. Liu, C. Zhang, L. Chen, G. Zhou, G. Nie, H. Yan, B. Ding, Y. Zhao, A DNA nanorobot functions as a cancer therapeutic in response to a molecular trigger in vivo. *Nat. Biotechnol.* **36**, 258–264 (2018).
20. S. Y. S. Wang, A. D. Ellington, Pattern generation with nucleic acid chemical reaction networks. *Chem. Rev.* **119**, 6370–6383 (2019).
21. F. C. Simmel, B. Yurke, H. R. Singh, Principles and applications of nucleic acid strand displacement reactions. *Chem. Rev.* **119**, 6326–6369 (2019).
22. D. Wang, R. Peng, Y. Peng, Z. Deng, F. Xu, Y. Su, P. Wang, L. Li, X.-Q. Wang, Y. Ke, W. Tan, Hierarchical fabrication of DNA wireframe nanoarchitectures for efficient cancer imaging and targeted therapy. *ACS Nano* **14**, 17365–17375 (2020).
23. M. Li, H. Ding, M. Lin, F. Yin, L. Song, X. Mao, F. Li, Z. Ge, L. Wang, X. Zuo, Y. Ma, C. Fan, DNA framework-programmed cell capture via topology-engineered receptor-ligand interactions. *J. Am. Chem. Soc.* **141**, 18910–18915 (2019).
24. D. Wang, S. Li, Z. Zhao, X. Zhang, W. Tan, Engineering a second-order DNA logic-gated nanorobot to sense and release on live cell membranes for multiplexed diagnosis and synergistic therapy. *Angew. Chem. Int. Ed.* **60**, 15816–15820 (2021).
25. Y. F. Lyu, C. C. Wu, C. Heinke, D. Han, R. Cai, I. T. Teng, Y. Liu, H. Liu, X. B. Zhang, Q. L. Liu, W. H. Tan, Constructing smart protocells with built-in DNA computational core to eliminate exogenous challenge. *J. Am. Chem. Soc.* **140**, 6912–6920 (2018).
26. D. Han, C. Wu, M. You, T. Zhang, S. Wan, T. Chen, L. Qiu, Z. Zheng, H. Liang, W. Tan, A cascade reaction network mimicking the basic functional steps of adaptive immune response. *Nat. Chem.* **7**, 835–841 (2015).
27. M. Rudchenko, S. Taylor, P. Pallavi, A. Dechkovskaia, S. Khan, V. P. Butler Jr., S. Rudchenko, M. N. Stojanovic, Autonomous molecular cascades for evaluation of cell surfaces. *Nat. Nanotechnol.* **8**, 580–586 (2013).
28. R. Peng, L. Xu, H. Wang, Y. Lyu, D. Wang, C. Bi, C. Cui, C. Fan, Q. Liu, X. Zhang, W. Tan, DNA-based artificial molecular signaling system that mimics basic elements of reception and response. *Nat. Commun.* **11**, 978 (2020).
29. L. Yang, Y. Zhao, X. Xu, K. Xu, M. Zhang, K. Huang, H. Kang, H. C. Lin, Y. Yang, D. Han, An intelligent DNA nanorobot for autonomous anticoagulation. *Angew. Chem. Int. Ed.* **59**, 17697–17704 (2020).
30. D. Han, Z. Zhu, C. C. Wu, L. Peng, L. J. Zhou, B. Gulbakan, G. Z. Zhu, K. R. Williams, W. H. Tan, A logical molecular circuit for programmable and autonomous regulation of protein activity using DNA aptamer–protein interactions. *J. Am. Chem. Soc.* **134**, 20797–20804 (2012).
31. K. M. Cherry, L. Qian, Scaling up molecular pattern recognition with DNA-based winner-take-all neural networks. *Nature* **559**, 370–376 (2018).
32. D. Woods, D. Doty, C. Myhrvold, J. Hui, F. Zhou, P. Yin, E. Winfree, Diverse and robust molecular algorithms using reprogrammable DNA self-assembly. *Nature* **567**, 366–372 (2019).
33. Y. J. Chen, N. Dalchau, N. Srinivas, A. Phillips, L. Cardelli, D. Soloveichik, G. Seelig, Programmable chemical controllers made from DNA. *Nat. Nanotechnol.* **8**, 755–762 (2013).
34. U. Alon, Network motifs: Theory and experimental approaches. *Nat. Rev. Genet.* **8**, 450–461 (2007).
35. S. Mangan, U. Alon, Structure and function of the feed-forward loop network motif. *Proc. Natl. Acad. Sci. U.S.A.* **100**, 11980–11985 (2003).
36. J. Liu, F. Li, Y. Wang, L. Pan, P. Lin, B. Zhang, Y. Zheng, Y. Xu, H. Liao, G. Ko, F. Fei, C. Xu, Y. Du, K. Shin, D. Kim, S. S. Jang, H. J. Chung, H. Tian, Q. Wang, W. Guo, J. M. Nam, Z. Chen, T. Hyeon, D. Ling, A sensitive and specific nanosensor for monitoring extracellular potassium levels in the brain. *Nat. Nanotechnol.* **15**, 321–330 (2020).
37. Z. Wang, T. C. Detomasi, C. J. Chang, A dual-fluorophore sensor approach for ratiometric fluorescence imaging of potassium in living cells. *Chem. Sci.* **12**, 1720–1729 (2020).
38. P. Yin, H. M. Choi, C. R. Calvert, N. A. Pierce, Programming biomolecular self-assembly pathways. *Nature* **451**, 318–322 (2008).
39. Y. Zhang, Y. Yan, W. Chen, W. Cheng, S. Li, X. Ding, D. Li, H. Wang, H. Ju, S. Ding, A simple electrochemical biosensor for highly sensitive and specific detection of microrna based on mismatched catalytic hairpin assembly. *Biosens. Bioelectron.* **68**, 343–349 (2015).

40. Y. S. Jiang, S. Bhadra, B. Li, A. D. Ellington, Mismatches improve the performance of strand-displacement nucleic acid circuits. *Angew. Chem. Int. Ed.* **53**, 1845–1848 (2014).

41. R. R. Machinek, T. E. Ouldridge, N. E. Haley, J. Bath, A. J. Turberfield, Programmable energy landscapes for kinetic control of DNA strand displacement. *Nat. Commun.* **5**, 5324 (2014).

42. W. Zhang, R. Taheri-Ledari, Z. Hajizadeh, E. Zolfaghari, M. R. Ahghari, A. Maleki, M. R. Hamblin, Y. Tian, Enhanced activity of vancomycin by encapsulation in hybrid magnetic nanoparticles conjugated to a cell-penetrating peptide. *Nanoscale* **12**, 3855–3870 (2020).

43. H. C. Ates, J. A. Roberts, J. Lipman, A. E. G. Cass, G. A. Urban, C. Dincer, On-site therapeutic drug monitoring. *Trends Biotechnol.* **38**, 1262–1277 (2020).

44. P. Dauphin-Ducharme, K. Yang, N. Arroyo-Curras, K. L. Ploense, Y. Zhang, J. Gerson, M. Kurnik, T. E. Kippin, M. N. Stojanovic, K. W. Plaxco, Electrochemical aptamer-based sensors for improved therapeutic drug monitoring and high-precision, feedback-controlled drug delivery. *ACS Sens.* **4**, 2832–2837 (2019).

45. J. R. Burns, A. Seifert, N. Fertig, S. Howorka, A biomimetic DNA-based channel for the ligand-controlled transport of charged molecular cargo across a biological membrane. *Nat. Nanotechnol.* **11**, 152–156 (2016).

46. C. Lanphere, D. Offenbartl-Stiegert, A. Dorey, G. Pugh, E. Georgiou, Y. Xing, J. R. Burns, S. Howorka, Design, assembly, and characterization of membrane-spanning DNA nanopores. *Nat. Protoc.* **16**, 86–130 (2021).

47. S. Pautot, B. J. Frisken, D. A. Weitz, Production of unilamellar vesicles using an inverted emulsion. *Langmuir* **19**, 2870–2879 (2003).

48. O. D. Toparlak, J. Zasso, S. Bridi, M. D. Serra, P. Macchi, L. Conti, M. L. Baudet, S. S. Mansy, Artificial cells drive neural differentiation. *Sci. Adv.* **6**, eabb4920 (2020).

49. Y. Zhang, Y. Chen, X. Yang, X. He, M. Li, S. Liu, K. Wang, J. Liu, S. Mann, Giant coacervate vesicles as an integrated approach to cytomimetic modeling. *J. Am. Chem. Soc.* **143**, 2866–2874 (2021).

50. A. Kato, M. Yanagisawa, Y. T. Sato, K. Fujiwara, K. Yoshikawa, Cell-sized confinement in microspheres accelerates the reaction of gene expression. *Sci. Rep.* **2**, 283 (2012).

51. T. Sunami, N. Ichihashi, T. Nishikawa, Y. Kazuta, T. Yomo, Effect of liposome size on internal RNA replication coupled with replicase translation. *Chembiochem* **17**, 1282–1289 (2016).

52. D. Y. Zhang, E. Winfree, Control of DNA strand displacement kinetics using toehold exchange. *J. Am. Chem. Soc.* **131**, 17303–17314 (2009).

53. L. Yue, S. Wang, V. Wulf, S. Lilienthal, F. Remacle, R. D. Levine, I. Willner, Consecutive feedback-driven constitutional dynamic networks. *Proc. Natl. Acad. Sci. U.S.A.* **116**, 2843–2848 (2019).

54. S. Krishnan, D. Ziegler, V. Arnaut, T. G. Martin, K. Kapsner, K. Henneberg, A. R. Bausch, H. Dietz, F. C. Simmel, Molecular transport through large-diameter DNA nanopores. *Nat. Commun.* **7**, 12787 (2016).

55. S. Dey, A. Dorey, L. Abraham, Y. Z. Xing, I. Zhang, F. Zhang, S. Howorka, H. Yan, A reversibly gated protein-transporting membrane channel made of DNA. *Nat. Commun.* **13**, 2271 (2022).

56. D. F. Babcock, G. A. Rufo Jr., H. A. Lardy, Potassium-dependent increases in cytosolic pH stimulate metabolism and motility of mammalian sperm. *Proc. Natl. Acad. Sci. U.S.A.* **80**, 1327–1331 (1983).

57. P. Wookey, P. Gupta, L. Bittencourt, S. Cheung, D. Hare, S. Furness, Methods to measure calcitonin receptor activity, up-regulated in cell stress, apoptosis and autophagy. *F1000Res* **10**, 1019 (2021).

58. K. Ohtsuka, S. Sato, Y. Sato, K. Sota, S. Ohzawa, T. Matsuda, K. Takemoto, N. Takamune, B. Juskowiak, T. Nagai, S. Takenaka, Fluorescence imaging of potassium ions in living cells using a fluorescent probe based on a thrombin binding aptamer-peptide conjugate. *Chem. Commun.* **48**, 4740–4742 (2012).

59. O. Vermesh, A. Aalipour, T. J. Ge, Y. Saenz, Y. Guo, I. S. Alam, S. M. Park, C. N. Adelson, Y. Mitsutake, J. Vilches-Moure, E. Godoy, M. H. Bachmann, C. C. Ooi, J. K. Lyons, K. Mueller, H. Arami, A. Green, E. I. Solomon, S. X. Wang, S. S. Gambhir, An intravascular magnetic wire for the high-throughput retrieval of circulating tumour cells in vivo. *Nat. Biomed. Eng.* **2**, 696–705 (2018).

60. K. Jahnke, V. Huth, U. Mersdorf, N. Liu, K. Gopfrich, Bottom-up assembly of synthetic cells with a DNA cytoskeleton. *ACS Nano* **16**, 7233–7241 (2022).

61. Y. Ouyang, P. Zhang, I. Willner, Dissipative biocatalytic cascades and gated transient biocatalytic cascades driven by nucleic acid networks. *Sci. Adv.* **8**, eabn3534 (2022).

62. E. Del Grosso, P. Irmisch, S. Gentile, L. J. Prins, R. Seidel, F. Ricci, Dissipative control over the toehold-mediated DNA strand displacement reaction. *Angew. Chem. Int. Ed.* **61**, e202201929 (2022).

63. M. Hadorn, E. Boenzli, K. T. Sorensen, D. De Lucrezia, M. M. Hanczyc, T. Yomo, Defined DNA-mediated assemblies of gene-expressing giant unilamellar vesicles. *Langmuir* **29**, 15309–15319 (2013).